Vietnam Journal of Mechanics, Vol. 48, No. 1 (2026), pp. 62 – 80
DOI: https://doi.org/10.15625/0866-7136/23632

COUPLED LATTICE BOLTZMANN–DISCRETE ELEMENT SIMULATIONS OF BED LOAD SEDIMENT TRANSPORT

Duc Chung Vu[1], **Thanh-Trung Vo**[2]
[1]*Faculty of Hydraulic Engineering, Hanoi University of Civil Engineering, Hanoi, Vietnam*
[2]*School of Transportation Engineering, Danang Architecture University, Danang, Vietnam*
E-mail: chungvd@huce.edu.vn

Received: 16 October 2025 / Revised: 5 January 2026 / Accepted: 20 January 2026
Published online: 29 March 2026

Abstract. The transport of granular bed under fluid flow involves erosion, entrainment, and deposition processes, that are fundamental to both geophysical and engineering systems. This study presents numerical simulations of bed load sediment transport induced by turbulent shear flow using a two-dimensional coupled framework that combines the lattice Boltzmann method (LBM) for the fluid phase with the discrete element method (DEM) for granular dynamics. A multiple-relaxation-time LBM is developed to enhance numerical stability without significantly increasing computational cost. First, the model is validated against two classical benchmark tests, showing excellent agreement with the analytical and numerical references. Subsequently, simulations of a polydisperse granular bed reveal three distinct regions: a bedload layer, where particles roll and slide at low velocities through frictional contacts; a saltation layer, where particles are intermittently lifted and redeposited; and a suspension layer, where particles are transported by the flow, with their velocities approaching the maximum fluid velocity. Furthermore, the force-chain structure in the bedload layer is analogous to that observed in dry granular packing under simple shear, despite the differences in particle shape. The simulations data further demonstrate size-dependent segregation within the bedload layer, driven by shear-induced particle interactions.

Keywords: bed load sediment transport, turbulent shear flow, coupled lattice Boltzmann–discrete element simulation, multiple-relaxation-time model, size-dependent particle segregation.

1. INTRODUCTION

Turbulent shear flow acting on an erodible granular bed drives sediment transport, a process that fundamentally shapes the morphology of rivers and coastal environments. This process is known to influence landscape evolution, water quality, fluvial ecosystems, and public safety (Deal et al., 2023; Dedieu et al., 2024; Schmeeckle, 2014). Despite its ubiquity in natural environments and nearly a century of intensive investigation into bed load transport, the fundamental mechanisms governing fluid-sediment interactions remain incompletely understood (Deal et al., 2023; Pähtz et al., 2020; Zhang et al., 2020). Furthermore, because sediment transport is ultimately controlled by the hydrologic cycle, variations in climate directly influence sediment dynamics, thereby adding further complexity to the prediction of river behavior (Deal et al., 2023; Raymond Pralong et al., 2015). Sediment entrainment begins once the hydrodynamic forces imposed on a particle exceed the resisting forces arising from gravity and interparticle friction. Following entrainment, sediment particles move downstream, leading to the bed load transport stage, characterized by rolling and sliding of particles in the bedload layer. Under conditions of sufficiently intense turbulence, this regime may evolve into saltation where particles are lifted off the bed by fluid forces and then fall back down after traveling a short distance.

Subsequently, with a further increase in turbulence, sediment particles are carried along with the stream in a suspension state (Guazzelli & Pouliquen, 2018; Ji et al., 2013; Ji et al., 2014).

One of the key processes relevant to bedload sediment transport is size segregation, which can occur in two distinct forms (Frey & Church, 2009; Li et al., 2010). When the largest particles of the bed remain immobile and the smallest particles are sufficiently fine, the latter may migrate downward by spontaneous percolation, moving through the voids between larger particles. In contrast, once the bed is in motion, meaning that both large and small particles move under shear, segregation is dominated by a kinematic sieving process, whereby transient voids created by particle rearrangement permit finer particles to descend even at particle size ratios approaching unity. Together, these mechanisms generate a reorganization of particle sizes within deposits and produce the vertical size segregation commonly observed in riverbeds (Frey & Church, 2009; Gonzalez et al., 2023). Size segregation within the granular bed has been recognized as a significant contributor to bed hardening, which is defined as the gradual increase in the critical shear stress necessary to initiate bed load transport (Charru et al., 2004; Masteller & Finnegan, 2017; Masteller et al., 2019). Although previous works have advanced our knowledge of size segregation dynamics in particle-laden flow under shear, several important aspects remain poorly understood, such as the mesoscale structure and evolution of shear-induced hardening in polydisperse beds, and the quantitative properties of segregation rates across flow regimes.

Modeling sediment transport at the continuum scale requires a two-phase framework, wherein both the fluid and granular phases are characterized by appropriate constitutive stress relations. Over recent decades, a wide range of numerical strategies has been developed to describe such systems, including Eulerian two-phase continuous models (van der Hoef et al., 2008), hybrid Eulerian-Lagrangian couplings such as computational fluid dynamics (CFD)–discrete element method (DEM) (Elghannay & Tafti, 2018; Gonzalez & Franklin, 2024; Ji et al., 2014; Nguyen et al., 2025; Schmeeckle, 2014), and more recently, lattice Boltzmann method (LBM)–DEM approaches that resolve fluid-particle interactions at finer scales (Amarsid et al., 2017; Mutabaruka et al., 2014; Ngoma et al., 2018).

Rather than directly solving the Navier–Stokes equations as in traditional CFD solvers, the lattice Boltzmann method uses a mesoscopic formulation in which fluid behavior is represented by particle distribution functions. It offers several advantages, such as simple coding, easy implementation of boundary conditions, and full parallelism. Consequently, the coupling of LBM with DEM has become an efficient approach for simulating fluid-particle interactions (Boutt et al., 2011; Boutt et al., 2007; Owen et al., 2011), particularly in soil mechanics problems including porous flows (Y. Han & Cundall, 2013), submarine avalanches (Bigot et al., 2014; Mutabaruka et al., 2014), and sediment transport (Derksen, 2011; Harshani et al., 2015; Lominé et al., 2013).

This paper presents simulations of bed load sediment transport driven by turbulent shear flow using a coupled lattice Boltzmann–discrete element approach. By examining particle velocities, vertical trajectories, the evolution of the contact-force network, and the fluid velocity field, we show that the granular bed naturally separates into three distinct regions, namely bedload, saltation, and suspension layers. The phenomenon of size segregation is also observed in our simulations. These results demonstrate the capability of our numerical code to accurately model particle-laden flows. The paper is structured as follows. Section 2 describes the core aspects of the numerical methodology, including concise explanations of the lattice Boltzmann method, the discrete element method, and how the two are coupled. Following that, Section 3 introduces two validation tests for the standalone LBM and the coupled LBM-DEM model. The application of the model to bed load sediment transport and the corresponding numerical results are presented in Section 4. Finally, we summarize and discuss the key findings of this study in Section 5.

2. NUMERICAL METHOD

2.1. Multiple-relaxation-time lattice Boltzmann method

The lattice Boltzmann method (LBM) is a numerical approach for modeling quasi-incompressible fluid flows and serves as an alternative to conventional computational fluid dynamics (CFD) methods that directly solve the Navier–Stokes equations. Rooted in kinetic theory, the LBM is derived from the mesoscopic Boltzmann equation, which describes the flow in terms of the probability of finding a particle in a given state. In this framework, the hydrodynamics of a fluid are captured by treating it as a collection of particles whose dynamics follow the Boltzmann equation. The fundamental variable is the particle distribution function $f(\vec{x},\vec{c},t)$ which contains information about the mesoscopic state of the fluid. The LBM is discretized on a regular lattice using a finite set of discrete velocity directions $\vec{e}_i$ and corresponding velocity vectors $\vec{c}_i = c\vec{e}_i$. The discretized form of the Boltzmann equation is then expressed as

$$\frac{\partial f_i(\vec{x},\vec{c},t)}{\partial t} + \vec{c}_i \cdot \vec{\nabla} f_i(\vec{x},\vec{c},t) = \Omega_i, \tag{1}$$

where $f_i(\vec{x},\vec{c},t)$ is the distribution function corresponding to direction i, Ω_i represents the relevant collision operator, and $\vec{c}$ indicates the lattice velocity term.

The LBM employs a discrete formulation of Eq. (1) through specific discretization in both time and space, given by (He & Luo, 1997a, 1997b; Krüger et al., 2017; Succi, 2018)

$$f_i(\vec{x}+\vec{c}_i\Delta t, t+\Delta t) - f_i(\vec{x},t) = \Omega_i, \tag{2}$$

where the lattice velocity c and the time increment Δt satisfy $c = \Delta x/\Delta t$, with Δx as the lattice spacing. Accordingly, a fluid particle either stays put ($\vec{c}_0 = \vec{0}$) or moves to an adjacent node along direction $\vec{e}_i$ during a single time step. In lattice units, one sets $\Delta x = \Delta t = c = 1$, normalizing space and time. The lattice Boltzmann formulation is thus commonly written in lattice units, allowing all variables to be dimensionless and simplifying its implementation.

The simulations utilized the D2Q9 lattice scheme, where the domain is discretized into square lattice cells. Each node holds distribution functions f_i corresponding to the density of fluid particles moving along the nine discrete velocity directions $\vec{c}_i$, as shown in Fig. 1. The D2Q9 model is widely adopted because it provides an excellent balance between computational efficiency and numerical accuracy, while ensuring good isotropy for simulating two-dimensional fluid flows. The discrete velocity set is given by

$$\vec{c}_i = \begin{cases} (0,0) & \text{for } i = 0, \\ (\cos[(i-1)\pi/2], \sin[(i-1)\pi/2]) & \text{for } i = 1-4, \\ (\cos[(2i-9)\pi/4], \sin[(2i-9)\pi/4])\sqrt{2} & \text{for } i = 5-8. \end{cases} \tag{3}$$

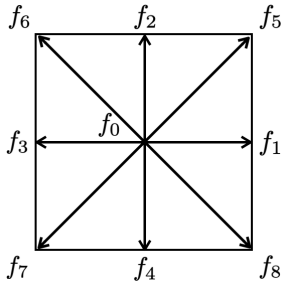

Fig. 1. The square lattice cell of the D2Q9 model indicating the orientation of its nine discrete distribution functions

At each node, the macroscopic fluid quantities such as the density ρ and the velocity $\vec{u}$ can be calculated from the moments of the distribution functions. In lattice units, we have

$$\rho = \sum_{i=0}^{8} f_i, \tag{4}$$

and

$$\rho\vec{u} = \sum_{i=0}^{8} f_i\vec{e}_i. \tag{5}$$

Assuming the fluid is incompressible, the pressure p is calculated directly from the density via the following ideal fluid equation of state,

$$p = c_s^2\rho, \tag{6}$$

where c_s denotes the speed of sound in the fluid, which in the D2Q9 model is defined as $c_s = c/\sqrt{3}$.

Several methods exist to approximate the collision operator, with one of the most common being the Bhatnagar–Gross–Krook (BGK) or single-relaxation-time model proposed by Bhatnagar et al. (1954). In this model, for each direction i, the distribution function $f(\vec{x}, t)$ relaxes linearly toward its local equilibrium $f^{eq}(\vec{x}, t)$ over a characteristic time τ, giving the collision operator Ω_i as

$$\Omega_i = -\frac{1}{\tau}\left[f_i(\vec{x}, t) - f_i^{eq}(\vec{x}, t)\right]. \tag{7}$$

A second-order Taylor expansion of the Maxwell equilibrium distribution is used to derive the equilibrium distribution function, leading to an expression formulated in terms of the macroscopic fluid properties (Krüger et al., 2017)

$$f_i^{eq}(\rho, \vec{u}) = \omega_i\rho\left[1 + 3(\vec{e}_i \cdot \vec{u}) + \frac{9}{2}(\vec{e}_i \cdot \vec{u})^2 - \frac{3}{2}\vec{u}^2\right], \tag{8}$$

where ω_i denotes the weight factor determined by the lattice configuration. In the D2Q9 model, $\omega_i = 4/9$ for $|\vec{c}_i| = 0$, $\omega_i = 1/9$ for $|\vec{c}_i| = 1$, and $\omega_i = 1/36$ for $|\vec{c}_i| = \sqrt{2}$. The relaxation time τ is related to the fluid kinematic viscosity ν by

$$\nu = \frac{2\tau - 1}{6}. \tag{9}$$

The discretized equations along the different lattice directions are solved in two successive steps. The first step, referred to as the collision step, accounts for the interactions among fluid particles and is conducted as follows:

$$f_i^{out}(\vec{x}, t) = f_i(\vec{x}, t) + \Omega_i, \tag{10}$$

where f_i^{out} denotes the postcollision distribution function. Secondly, the post-collision distribution functions are streamed along each lattice direction i. This streaming step is expressed as follows:

$$f_i(\vec{x} + \vec{c}_i\Delta t, t + \Delta t) = f_i^{out}(\vec{x}, t). \tag{11}$$

In the BGK model, all physical variables are relaxed with a single characteristic time τ, which is simple but may lead to fluctuations in the velocity field. In the present simulations, a multiple-relaxation-time (MRT) collision scheme was adopted instead (Lallemand & Luo, 2000; Peng et al., 2016). Through the transformation matrix $\boldsymbol{\mathcal{M}}$, this approach maps the nine distribution functions at each fluid node to nine independent moments, such that

$$\boldsymbol{m} = \boldsymbol{\mathcal{M}}\boldsymbol{f}, \tag{12}$$

where the transpose matrix of $\boldsymbol{m}^T = (m_0, m_1, ..., m_8)$ is the vector of moments, the transpose matrix of $\boldsymbol{f}^T = (f_0, f_1, ..., f_8)$ is the vector of distribution functions, and the transformation matrix $\boldsymbol{\mathcal{M}}$ takes the form

$$\boldsymbol{\mathcal{M}} = \begin{bmatrix} 1 & 1 & 1 & 1 & 1 & 1 & 1 & 1 & 1 \\ -4 & -1 & 2 & -1 & 2 & -1 & 2 & -1 & 2 \\ 4 & -2 & 1 & -2 & 1 & -2 & 1 & -2 & 1 \\ 0 & 1 & 1 & 0 & -1 & -1 & -1 & 0 & 1 \\ 0 & -2 & 1 & 0 & -1 & 2 & -1 & 0 & 1 \\ 0 & 0 & 1 & 1 & 1 & 0 & -1 & -1 & -1 \\ 0 & 0 & 1 & -2 & 1 & 0 & -1 & 2 & -1 \\ 0 & 1 & 0 & -1 & 0 & 1 & 0 & -1 & 0 \\ 0 & 0 & 1 & 0 & -1 & 0 & 1 & 0 & -1 \end{bmatrix}. \tag{13}$$

Accordingly, collisions are executed in the moment space, with each moment m_i relaxing toward its equilibrium m_i^{eq} at a rate defined by s_i. The resulting post-collision moment vector $\boldsymbol{m}^{out}$ is given by

$$\boldsymbol{m}^{out} = \boldsymbol{m} - \boldsymbol{S}(\boldsymbol{m} - \boldsymbol{m}^{eq}), \tag{14}$$

where $\boldsymbol{S} = (0, s_1, s_2, 0, s_4, 0, s_6, s_7, s_8)^T$ is a diagonal 9×9 matrix. In our simulations, we used the values of the relaxation time s_i as proposed by Mussa et al. (2009), in which $s_1 = 1.63$, $s_2 = 1.14$, $s_4 = s_6 = 1.92$, and $s_7 = s_8 = 1/\tau$. The equilibrium moment vector $\boldsymbol{m}^{eq}$ is expressed as follows

$$\boldsymbol{m}^{eq} = \begin{bmatrix} \rho \\ -2\rho + 3(j_x^2 + j_y^2)/\rho \\ \rho - 3(j_x^2 + j_y^2)/\rho \\ j_x \\ -j_x \\ j_y \\ -j_y \\ (j_x^2 - j_y^2)/\rho \\ j_x j_y/\rho, \end{bmatrix}, \tag{15}$$

where $j_x = \rho u_x$, $j_y = \rho u_y$ is the flux vector. The distribution functions f_i^{out} resulting from the collision step are given by $\boldsymbol{f}^{out} = \boldsymbol{\mathcal{M}}^{-1}\boldsymbol{m}^{out}$. Finally, the streaming step is applied in the velocity space.

The no-slip boundary condition between the fluid and a stationary solid wall is imposed using the bounce-back rule. The principle of this boundary condition is that any particle distribution striking the wall during the streaming step is reflected back along its incoming direction. Note that the solid nodes are inactive, except for those at the boundary, which reflect all incoming distributions. The bounce-back boundary condition can be expressed as follows:

$$f_{-i}(\vec{x}_f, t + \Delta t) = f_i(\vec{x}_f, t), \tag{16}$$

where the notation $-i$ conventionally designates the velocity direction opposite to i, $\vec{x}_f$ is the position of the fluid node, and $f_i(\vec{x}_f, t)$ is the distribution function at the fluid node after collision (Krüger et al., 2017; Succi, 2018).

2.2. Discrete element method

The discrete element method (DEM) is a powerful and reliable computational technique for investigating granular and particulate systems. In this method, the motion of all particles, treated as rigid bodies, is obtained by integrating their equations of motion while accounting for both contact and external forces acting on them. From a technical standpoint, DEM is based on a temporally discretized formulation of the translational and rotational equations of

motion, combined with constitutive force laws that describe contact interactions through force-displacement relationships (Radjai & Dubois, 2011). The motion of each particle is governed by

$$\begin{cases} \hat{m}_i \dfrac{d^2\vec{r}_i}{dt^2} = \vec{F}_i + (\hat{m}_i - m_e)\vec{g}, \\ I_i \dfrac{d^2\vec{\varphi}_i}{dt^2} = \vec{T}_i, \end{cases} \tag{17}$$

where the symbols $\hat{m}_i$, I_i, $\vec{r}_i$, $\vec{\varphi}_i$ correspond to the mass, moment of inertia, position and orientation of particle i, $m_e\vec{g} = \rho\pi R^2\vec{g}$ is the buoyancy force, ρ is the fluid density, R is the particle radius, $\vec{g}$ is the gravitational acceleration, $\vec{F}_i$ and $\vec{T}_i$ are the total force and torque acting on the particle i, respectively. For each particle, Newton's equations of motion are solved numerically using an explicit time integration scheme, commonly referred to as the molecular dynamics (MD) method. In this study, the standard velocity-Verlet algorithm is used due to its numerical stability and simplicity. The total force $\vec{F}_i$ and torque $\vec{T}_i$ acting on particle i are expressed as

$$\vec{F}_i = \vec{F}_i^c + \vec{F}_i^h, \tag{18}$$

and

$$\vec{T}_i = \vec{T}_i^c + \vec{T}_i^h, \tag{19}$$

where $\vec{F}_i^c$ is the total force due to contacts with neighboring particles, while $\vec{F}_i^h$ is the hydrodynamic force from the fluid (see next section). The torques $\vec{T}_i^c$ and $\vec{T}_i^h$ correspond to contact- and fluid-induced contributions.

The contact force models commonly used in the DEM simulations have been extensively discussed in the literature (Cundall & Strack, 1979; Di Renzo & Di Maio, 2004; T. T. Vo et al., 2020; Vu et al., 2023, 2025). In the present study, a linear elastic contact law is adopted at each contact point between particles i and j. This model consists of a linear spring, a dashpot, and a shear slider acting on the contact point. The spring represents the elastic interaction between particles while the dashpot accounts for energy dissipation at the contact and the shear slider models the frictional force at the contact point.

Let $\vec{n}$ and $\vec{t}$ be the normal and tangential unit vectors at a contact point c between particles i and j. The force $\vec{F}^c = F_n\vec{n} + F_t\vec{t}$ acting by particle j on particle i at this contact point is expressed as a function of the normal relative displacement (overlap) δ_n and cumulative tangential displacement $\vec{\delta}_t$. The normal force law is expressed as (Radjai & Dubois, 2011; T.-T. Vo et al., 2023; Vu et al., 2023, 2024a, 2024b)

$$F_n = -k_n\delta_n - 2\alpha\sqrt{k_n\bar{m}}\,\dot{\delta}_n, \tag{20}$$

where k_n is the normal spring stiffness, δ_n is the normal displacement (with the sign convention that $\delta_n < 0$ is an overlap and $\delta_n > 0$ is a gap), $\dot{\delta}_n$ is the relative normal velocity, $\bar{m}$ is the reduced mass of the two particles in contact, and the dimensionless parameter α taking values between 0 and 1, models viscous damping and the associated dissipation of energy in the normal direction. Its value is a function of the normal restitution coefficient e_n (Brilliantov et al., 1996; Ismail & Stronge, 2008; Louge, 1994; Müller et al., 2012),

$$\alpha = \begin{cases} \dfrac{-\log e_n}{\sqrt{(\log e_n)^2 + \pi^2}} & \text{for } 0 < e_n \leq 1, \\ 1 & \text{for } e_n = 0. \end{cases} \tag{21}$$

For circular particles, the overlap between particles i and j is given by

$$\delta_n = |\vec{r}_i - \vec{r}_j| - (R_i + R_j), \tag{22}$$

where $\vec{r}_i$, $\vec{r}_j$ denote the positions of particles i and j, respectively, and R_i, and R_j are their corresponding radii.

The tangential component of the contact force is governed by the viscous-regularized Coulomb model (Amarsid et al., 2017; Mutabaruka et al., 2014; Ngoma et al., 2018),

$$\vec{F}_t = \begin{cases} k_t\vec{\delta}_t - 2\alpha\sqrt{k_n\bar{m}}\vec{v}_t & \text{if } |\vec{F}_t| \leq \mu_s F_n, \\ -\mu_s F_n \dfrac{\vec{v}_t}{|\vec{v}_t|} & \text{otherwise,} \end{cases} \tag{23}$$

where k_t is the tangential spring stiffness, and μ_s is the friction coefficient between particles. The direction of tangential force $\vec{t}$ is opposite to the relative elastic displacement $\vec{\delta}_t$ when the Coulomb threshold has not been reached, and opposite to the relative velocity $\vec{v}_t$ at the contact point once the Coulomb threshold is attained.

2.3. LBM-DEM coupling

In the coupled LBM-DEM framework, the interactions between the fluid and particles are explicitly computed through data exchange between the two methods. Typically, the hydrodynamic forces and torques derived from the LBM calculations are transferred to the DEM to update the positions and velocities of solid particles. Within the fluid domain, the particles are modeled as dynamic solid boundaries. They are discretized on the fluid lattice grid, with nodes corresponding to particle locations treated as solid nodes. The LBM-DEM coupling is then implemented by calculating the momentum exchange at the fluid-solid interfaces. The detailed implementation of this coupling scheme is illustrated in previous studies (Galindo-Torres, 2013; Y. Han & Cundall, 2013; Lallemand & Luo, 2003; Lominé et al., 2013; Mansouri et al., 2011).

In the present work, the interpolated bounce-back boundary condition proposed by Bouzidi et al. (2001) is imposed. Let q denote the normalized distance between the fluid node and the boundary surface, defined as $q = |\vec{x}_f - \vec{x}_w|/\Delta x$, where $\vec{x}_f$ and $\vec{x}_w$ are the position of fluid node and boundary surface, respectively, as shown in Fig. 2(a). The linear interpolation equations then depend on the value of q as follows:

$$f_{-i}(\vec{x}_f, t+\Delta t) = 2q f_i^{out}(\vec{x}_f, t) + (1-2q) f_i^{out}(\vec{x}_f - \vec{c}_i, t) + 6\omega_i \vec{c}_i \vec{u}_w \text{ for } q < 1/2, \tag{24}$$

$$f_{-i}(\vec{x}_f, t+\Delta t) = \frac{1}{2q} f_i^{out}(\vec{x}_f, t) + \frac{1-2q}{2q} f_i^{out}(\vec{x}_f - \vec{c}_i, t) + \frac{3}{q}\omega_i \vec{c}_i \vec{u}_w \text{ for } q \geq 1/2, \tag{25}$$

where $\vec{u}_w$ is the local velocity of the moving particle. The normalized distance q is computed as follows. Let $\boldsymbol{c}$ be the particle center, $\boldsymbol{o}$ and $\boldsymbol{f}$ be the positions of solid and fluid nodes, respectively (see Fig. 2(b)). We get the difference vector as $\vec{\ell} = \boldsymbol{o} - \boldsymbol{c}$. With $\vec{e}$ being the unit vector along the lattice link, we can write the intersection position as $\vec{x} = \boldsymbol{c} + \vec{\ell} + \alpha\vec{e}$, where α is the distance from $\boldsymbol{o}$ to the intersection point along $\vec{e}$. Because the intersection position is on a circle with center $\boldsymbol{c}$, we have $|\vec{x} - \boldsymbol{c}| = R^2$, leading to $|\vec{\ell} + \alpha\vec{e}| = R^2$. Noting that $\vec{e}$ is the unit length vector, we can simplify this equation in α as follows:

$$\alpha^2 + 2\alpha(\vec{\ell}\cdot\vec{e}) + (\vec{\ell}\cdot\vec{\ell} - R^2) = 0. \tag{26}$$

Eq. (26) can be solved to give the value of α as follows:

$$\alpha = \sqrt{(\vec{\ell}\cdot\vec{e})^2 - \vec{\ell}\cdot\vec{\ell} + R^2} - \vec{\ell}\cdot\vec{e}. \tag{27}$$

Furthermore, from Fig. 2(b) one gets $b = \vec{\ell}\cdot\vec{e}$, and $m^2 = \vec{\ell}\cdot\vec{\ell} - b^2$. Eq. (27) becomes

$$\alpha = \sqrt{R^2 - m^2} - b. \tag{28}$$

From the definition of q, one gets

$$q = 1 - \frac{\alpha}{\Delta x}. \tag{29}$$

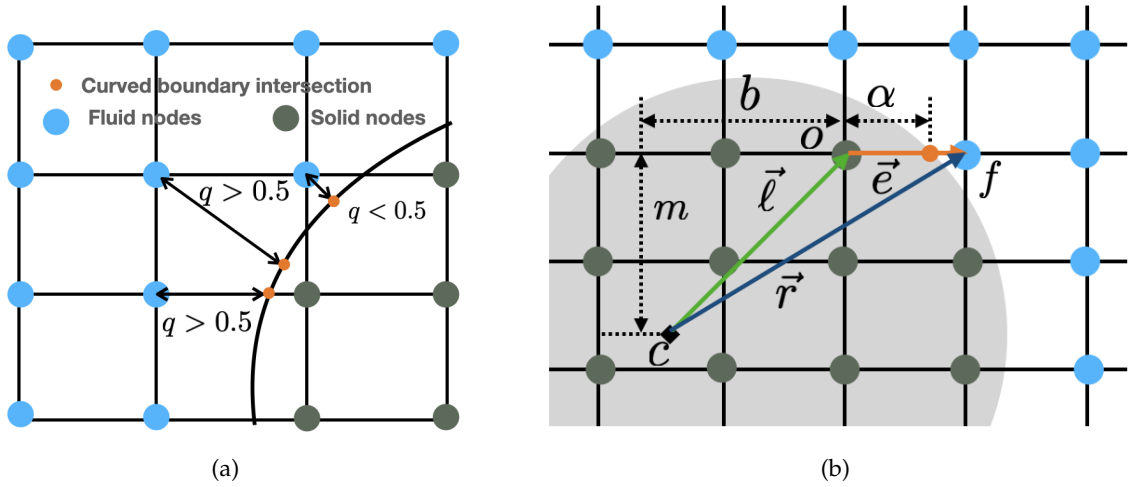

(a) (b)

Fig. 2. Lattice intersection between fluid and solid nodes for curved boundary (a). Intersection calculation for lattice nodes and a disk (b)

The effect of the fluid on a solid particle is accounted for through the hydrodynamic force $\partial\vec{F}^h$. This force is applied directly at the particle's center of mass. This force is computed using Ladd's method (Ladd, 1994), which calculates momentum transfer across the fluid-solid interface. In the streaming step, the partial distribution $f_i(\vec{x}_f, t)$ at a fluid node next to the interface is reflected, yielding $f_{-i}(\vec{x}_f, t + \Delta t)$. The hydrodynamic force is then expressed as (Y. T. Feng et al., 2007; Z.-G. Feng & Michaelides, 2004; Galindo-Torres, 2013; K. Han et al., 2007; Ladd & Verberg, 2001; Lallemand & Luo, 2003; Mansouri et al., 2011; Wen et al., 2014)

$$\partial\vec{F}^h = (f_{-i}(\vec{x}_f, t + \Delta t) + f_i(\vec{x}_f, t))\vec{c}_i. \tag{30}$$

3. VALIDATION AND BENCHMARKING

Before presenting the numerical results on bed load sediment transport, we examine the accuracy of the LBM and the coupled LBM-DEM method using the multiple-relaxation-time (MRT) model through two standard benchmark flows. As a first test, the LBM-MRT scheme is applied to the two-dimensional Couette flow, and the results are validated against the analytical solution. Subsequently, the effectiveness of the hydrodynamic coupling is demonstrated by simulating the 2D migration of a neutrally buoyant particle in a double Couette flow, with the results compared against previous numerical studies.

3.1. Couette flow

In fluid dynamics, Couette flow refers to the laminar motion of a viscous fluid confined between two infinite, parallel plates by a distance H. The upper plate moves with a constant velocity U_w, while the lower plate remains stationary. By solving the steady-state Navier–Stokes equations for simple shear flow without a pressure gradient in the flow direction, one obtains

$$\frac{u}{U_w} = \frac{y}{H}, \tag{31}$$

where u denotes the fluid velocity in the horizontal direction, while the vertical component is assumed to be zero. Consequently, the boundary conditions are $u = 0$ at $y = 0$ and $u = U_w$ at $y = H$.

In the LBM algorithm, the solid nodes moving with a constant velocity $\vec{u} = (u_x, 0)$ are imposed by the Neumann boundary condition (Zou & He, 1997). We consider fluid node A which is a neighbour of solid nodes as shown in Fig. 3. Due to the no-slip boundary condition,

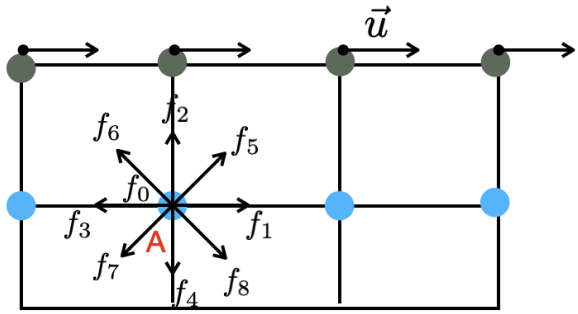

Fig. 3. Domain definition for velocity imposed conditions

node A also moves with velocity $\vec{u} = (u_x, 0)$. After the streaming step, the distribution function f_0, f_1, f_2, f_3, f_5, f_6 are known. We need to determine ρ, f_4, f_7, f_8. From Eqs. (4) and (5), one gets the following relation

$$\begin{aligned} \rho &= (f_0 + f_1 + f_3) + (f_2 + f_5 + f_6) + (f_4 + f_7 + f_8), \\ \rho u_x &= (f_1 + f_5 + f_8) - (f_3 + f_6 + f_7), \\ 0 &= (f_2 + f_5 + f_6) - (f_4 + f_7 + f_8). \end{aligned} \tag{32}$$

To close the system, we assume the bounce-back rule is still correct for the non-equilibrium part of the distribution function normal to the velocity direction, we have $f_4 - f_4^{eq} = f_2 - f_2^{eq}$. From Eq. (8), we get $f_4^{eq} = f_2^{eq}$, leading to $f_4 = f_2$. Combining with Eq. (32), one gets

$$\begin{aligned} \rho &= (f_0 + f_1 + f_3) + 2(f_2 + f_5 + f_6), \\ f_4 &= f_2, \\ f_8 &= f_6 + \frac{1}{2}\rho u_x + \frac{1}{2}(f_3 - f_1), \\ f_7 &= f_5 - \frac{1}{2}\rho u_x + \frac{1}{2}(f_1 - f_3). \end{aligned} \tag{33}$$

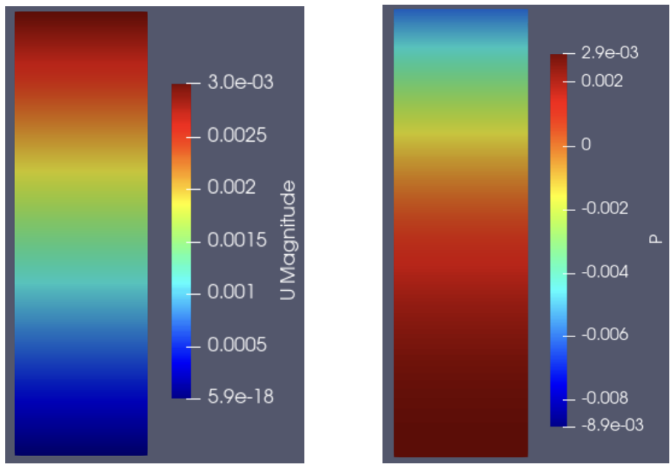

(a) (b)

Fig. 4. Fluid velocity along flow direction (a) and the pressure (b) at the steady state of the Couette flow

Fig. 4 displays the steady-state velocity and pressure profiles of the Couette flow. However, the steady state is not reached instantaneously. The transient (start-up) behavior describing the evolution toward steady state is also governed by the Navier–Stokes equation, which can be expressed as

$$u = U_w \mathrm{erfc}\left(\frac{y}{2\sqrt{\nu t}}\right), \tag{34}$$

where the complementary error function is given by

$$\mathrm{erfc}(z) = 1 - \mathrm{erf}(z) = \frac{2}{\sqrt{\pi}} \int_z^\infty e^{-t^2} dt. \tag{35}$$

Fig. 5 illustrates the relaxation process toward the steady state, which is obtained after approximately 20 seconds. The time required to reach the steady state depends solely on the plate spacing H and the kinematic viscosity of the fluid, but not on the velocity of moving plate U_w.

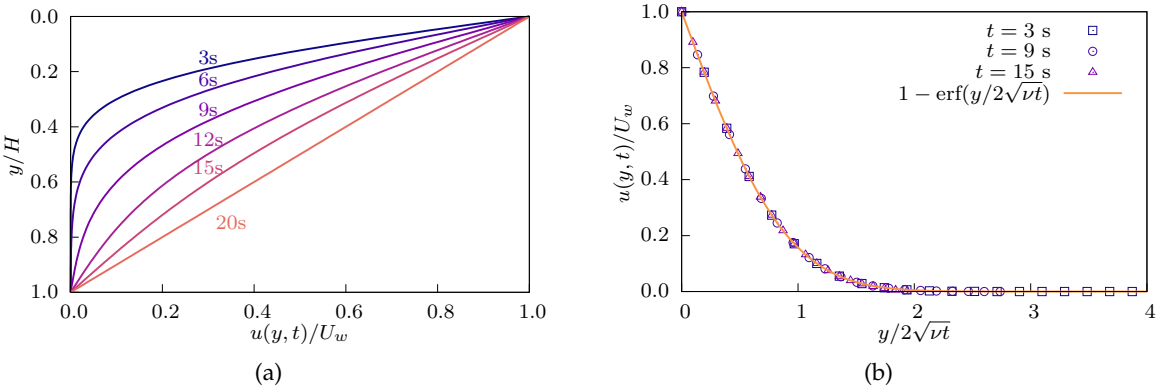

Fig. 5. Evolution of the fluid velocity as a function of time during the startup of Couette flow (a). Time scale of the Couette flow depending on the error function as shown in Eq. (34)

3.2. Migration of a neutrally buoyant particle in a simple shear flow

The motion of a neutrally buoyant 2D circular particle in a viscous fluid has been extensively investigated using numerical simulations based on the LBM (Z.-G. Feng & Michaelides, 2004; Niu et al., 2006) and the finite element method (FEM) (J. Feng et al., 1994). Therefore, comparing the present results with those obtained from these well-established methods provides an additional validation of the proposed LBM-DEM coupling approach. A schematic of the neutrally buoyant particle in a linear shear flow is shown in Fig. 6.

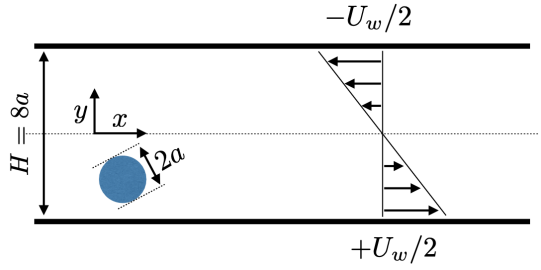

Fig. 6. Schematic diagram of a neutrally buoyant particle in a simple shear flow between two parallel walls

In the LBM framework, two unit systems are typically employed: the lattice unit system and physical unit system. Because the mechanical response is independent of the unit system, the simulation parameters are presented in lattice units for convenience. The channel height and length are set to $H = 80$ and $L = 2000$, respectively, while the particle diameter is $d = 2a = 0.25H$. The double Couette flow is imposed, with the upper and lower walls moving in opposite directions at velocities of $U_w/2 = 0.05$. The densities of particles and fluid are equal, $\rho_s = \rho_f = 1$, and the Reynolds number is $Re = U_w H/\nu = 40$. Periodic boundary conditions are applied at the inlet and outlet of the channel. The relaxation time is set to $\tau = 1.1$, corresponding to a fluid kinematic viscosity of $\nu = 0.2$. Initially, the particle is located at $y_0 = 0.25H$ above the bottom wall, halfway to the channel center, and is at rest. This results in a local slip velocity of $-0.25U_w$ relative to the fluid.

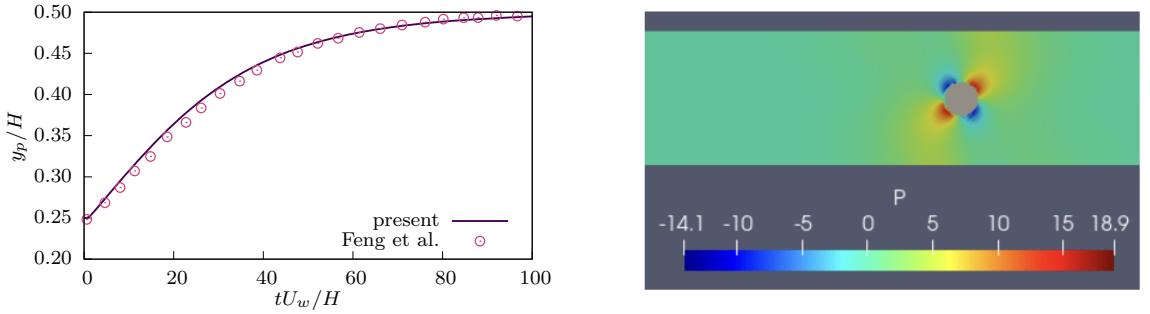

(a) (b)

Fig. 7. Lateral migration of the particle as a function of dimensionless time (a). The solid line indicates the simulation result of the present study while the symbols correspond to the numerical data reported by Z.-G. Feng and Michaelides (2004). Fluid pressure field around the particle at the equilibrium state (b)

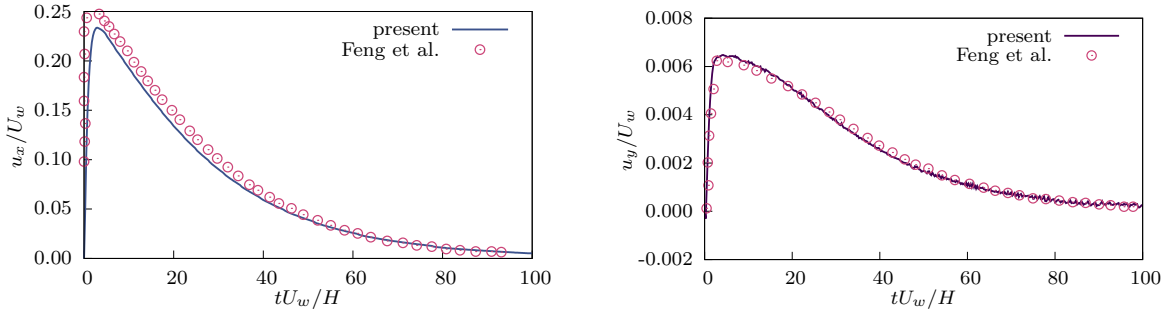

(a) (b)

Fig. 8. Particle translational velocity in the horizontal direction u_x (a) and vertical direction u_y (b) as functions of dimensionless time. The solid curves indicate the simulation result of the present study, while the data points show the numerical results of Z.-G. Feng and Michaelides (2004)

The lateral migration of the particle as a function of the dimensionless time $t^* = tU_w/H$ is displayed in Fig. 7(a), together with the numerical data reported by Z.-G. Feng and Michaelides (2004). The particle is observed to migrate toward the channel centerline, where it eventually reaches an equilibrium position. The present simulation results show excellent agreement with those of Z.-G. Feng and Michaelides (2004). Fig. 7(b) illustrates the fluid pressure field around the particle at equilibrium. As expected, the positive and negative pressure regions are symmetrically distributed about the centerline. Fig. 8 shows the horizontal and vertical components of

the particle velocity as a function of t^*. We see that both velocity components increase quickly to their peak values before gradually decreasing to zero as the particle approaches equilibrium. The maximum horizontal velocity u_x is approximately 40 times greater than the vertical velocity u_y. Overall, the present results are in very good agreement with those reported by Z.-G. Feng and Michaelides (2004).

4. SIMULATIONS OF BED LOAD SEDIMENT TRANSPORT

4.1. Numerical setup

Two-dimensional numerical simulations of bed load sediment transport under turbulent shear flow were conducted using the coupled LBM-DEM approach outlined earlier. The sediment particles were uniformly sized between $d_{\min} = 4$ mm and $d_{\max} = 10$ mm, with a uniform density of $\rho_g = 2600$ kg m^{-3}. A total of 240 particles were initially deposited under gravity within a domain of width $L = 0.304$ m and height $H = 0.06$ m. The friction coefficient between particles μ_s was set to 0.3 which is a typical value of friction coefficient in most granular materials (Tang et al., 2019). The normal spring stiffness was defined as $k_n = 5 \times 10^8$ N m^{-1}, while the tangential spring stiffness was set to $k_t = 0.8k_n$. To enhance contact dissipation, the restitution coefficient was set to a nearly inelastic value. In our simulations, the coefficient of restitution was equal to $e_n = 0.001$.

The fluid domain was divided into a square lattice of dimensions $L_x \times L_y = 1520 \times 300$ with an elementary spacing $\Delta x = 0.2$ mm or, equivalently, a spatial resolution $d_{\min}/\Delta x = 20$. The grid resolution used in this study is twice the value recommended by Ngoma et al. (2018) for similar Reynolds numbers, ensuring numerical independence with respect to spatial resolution. The whole domain is saturated with a fluid of viscosity $\nu = 10^{-5}$ m^2 s^{-1} and density $\rho_f = 1000$ kg m^{-3}. The no-slip bounce-back boundary condition was applied on the top and bottom walls of the computational domain. A uniform velocity gradient $\dot{\gamma} = U_w/H$ is applied to the fluid nodes on the left and right boundaries to generate a plane Couette flow. The fluid starts at rest, and the shear rate $\dot{\gamma}$ is gradually ramped to its final value. Turbulence is induced by setting the maximum velocity to $U_w = 1$ m s^{-1}, corresponding to a Reynolds number $Re = U_w H/\nu = 6000$. In addition, both the fluid and particles are treated as periodic along the flow, allowing them to re-enter the domain from the opposite side with the same velocity, orientation, and properties when leaving one side of the computational domain as shown in Fig. 9. The number of particles, particle size distribution and Reynolds number are chosen to reflect the compromise between computational cost and the need to maintain sufficient physical fidelity in the simulations.

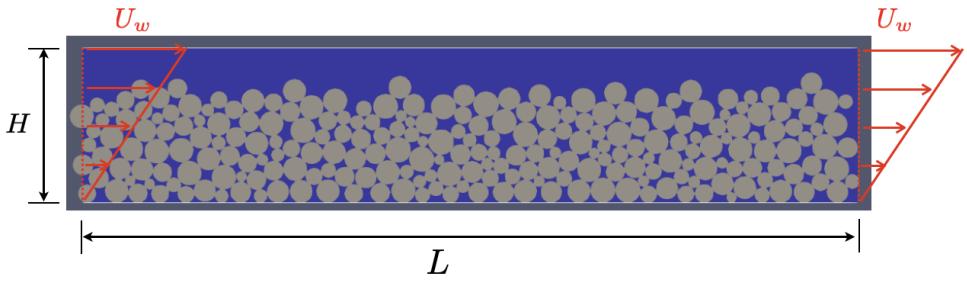

Fig. 9. Schematic of the geometry, boundary conditions, and computational domain under consideration

Apart from the lattice spacing Δx, the lattice speed c was set to 20 m s^{-1}, resulting in a time step $\Delta t = \Delta x/c = 1.5 \times 10^{-5}$ s. The integration was divided into $N_{sub} = 3$ substeps, such that the LBM time step was three times longer than the DEM time step. A larger value of N_{sub} can reduce computational cost and time. Since LBM updates are the most time-consuming part

of the simulation, we kept $N_{sub} = 3$ to ensure the numerical stability. As indicated by Eq. (9), because the fluid viscosity is always positive, the relaxation time τ must exceed 0.5. In our simulations, $\tau = 0.68$ which is sufficiently high and the use of the multiple-relaxation-time model ensures the numerical accuracy.

4.2. Results and discussion

Fig. 10 displays the fluid velocity field and particle velocities at the end of the simulation ($t = 50$ s). It can be observed that in the lower layer, both the fluid and particles exhibit relatively low velocities, with particle motion predominantly characterized by rolling and sliding interactions. In contrast, the upper layer displays higher fluid and particle velocities, leading to particle hopping and downstream transport with the flow. The present numerical method successfully reproduces the three modes of sediment entrainment driven by turbulent flow including bedload transport, where particles roll or slide along the bed, saltation where particles are intermittently lifted and redeposited downstream, and suspension, where particles are carried within the fluid due to sustained turbulent motion.

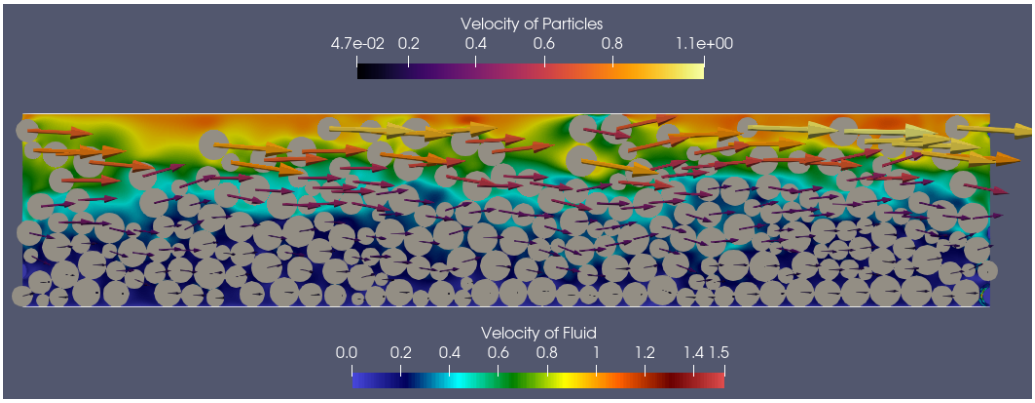

Fig. 10. Fluid velocity field and particle velocities at the end of the simulation. The length and color of arrows represent the particle velocity magnitude, whereas the fluid velocity is displayed by the color of the fluid surface

The temporal evolution of the vertical positions of six representative particles is presented in Fig. 11(a). These particles are initially located at different vertical layers. We see that the particle with ID = 32 primarily rolls and slides over the smooth wall, maintaining an almost constant vertical position throughout the simulation. The particle with ID = 90 interacts with neighboring particles and gradually sinks to a lower layer, whereas particle 49 moves upward slightly even though both are within the bedload layer and the initial position of particle 49 is lower than that of particle 90. This behavior reveals that depending on particle size, shear flow in the bedload layer can induce size segregation (Gonzalez & Franklin, 2024; Gonzalez et al., 2023). In contrast, particles with ID = 125 and 185 are lifted and transported by the stream within the suspension layers. Despite their different initial positions at $y/H = 0.4$ and $y/H = 0.6$, respectively, both particles reach a similar final vertical position of approximately $y/H = 0.65$. The particle with ID = 93 exhibits a typical saltation behavior, being periodically lifted off the bed and redeposited after traveling a short distance.

Fig. 11(b) shows the averaged velocity of particles as a function of the normalized vertical position across different layers. We see that the velocity profile can be divided into two distinct regions. From $y/H = 0$ to $y/H \simeq 0.55$, the velocity increases approximately linearly with height y/H from 0.15 to 0.28 m s^{-1}. In this range, the bed exhibits a fluid-like behavior corresponding to the bedload transport. At higher elevations, the particle velocity suddenly increases, approaching the applied flow velocity (1 m s^{-1}), as particles are entrained and carried

by the fluid stream. This upper region corresponds to the saltation and suspension regimes. Due to the turbulent nature of the flow and the limited bed thickness in the present setup, a creep or solid-like region, where particles move slowly and interact mainly through enduring frictional contacts, does not appear in this study.

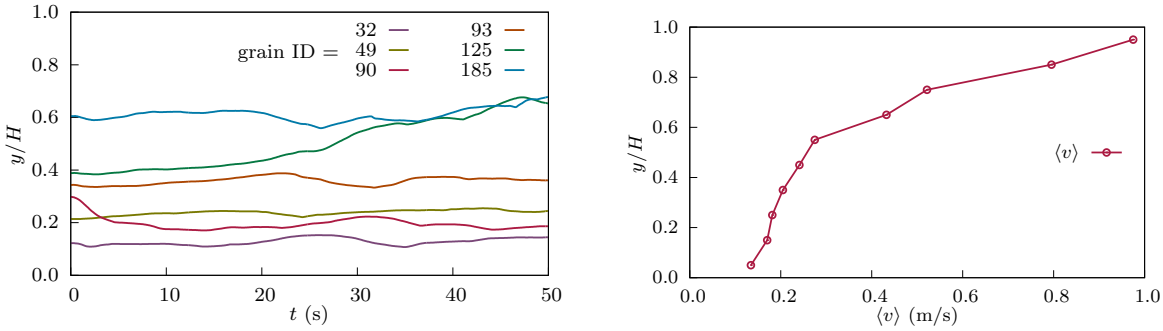

(a) (b)

Fig. 11. (a) Trajectories of six representative particles during the simulation. (b) Averaged particle velocity $\langle v \rangle$ as a function of the normalized vertical position across different layers

Fig. 12 displays the contact force network between particles arising from frictional interactions at the beginning and at the end of the simulation. Initially, the particles are randomly deposited within the computational domain, forming a relatively homogeneous force network as shown in Fig. 12(a). Once the fluid flow is imposed, this initial structure is disrupted, and the contact forces become mainly concentrated in the bedload layer. In contrast, within the saltation layer, particles collide intermittently while being transported by the fluid stream, as shown in Fig. 12(b). The strong force network is primarily oriented along a direction inclined at approximately 135° to the flow direction, resembling the force chain structure observed in dry granular packings subjected to simple shear, despite the differences in particle morphology (Azéma et al., 2015, 2018; Boton et al., 2013; Cantor et al., 2020).

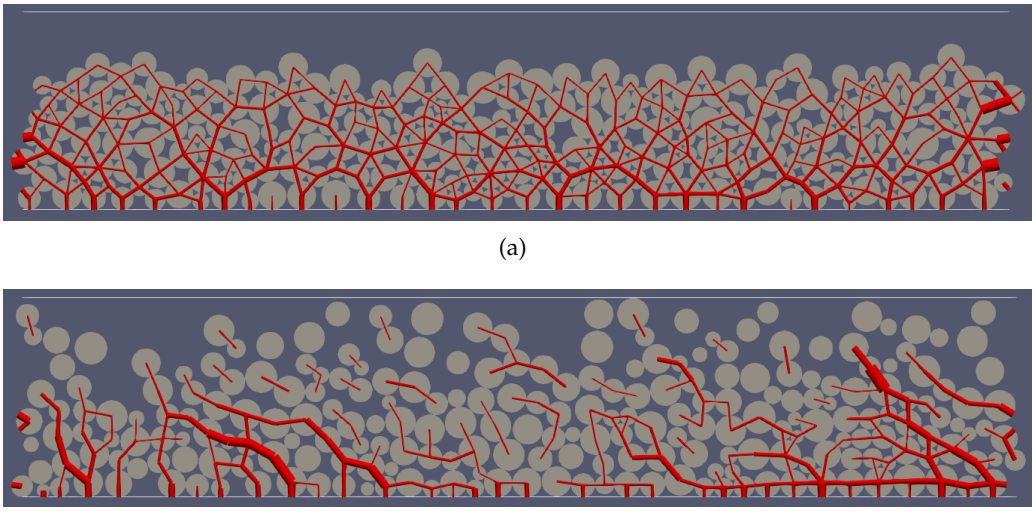

(a)

(b)

Fig. 12. Contact force network between particles at the beginning (a), and at the end of the simulation ($t = 50$ s) (b). Line thickness is proportional to the normal force

5. CONCLUSIONS

In this paper, a two-dimensional coupled LBM-DEM algorithm incorporating appropriate boundary conditions and collision model was employed to investigate bed load sediment transport driven by turbulent shear flow. The numerical model was first validated using two classical benchmark problems: Couette flow and the lateral migration of a neutrally buoyant particle in a double Couette flow. The simulation results show excellent agreement with analytical solutions and previous numerical studies, confirming the accuracy and stability of the model. Subsequently, we analyzed in detail the evolution of the granular bed velocity profile and vertical trajectories of particles at different layers. The simulation data indicate that the granular bed separates into three distinct regions: 1) a bedload layer, where particles roll and slide over one another at small velocities and the frictional contact network is concentrated; 2) a saltation layer, where particles are lifted off the bed and redeposited after traveling a short distance, and 3) a suspension layer, where particles are carried by the flow with their velocities approaching the imposed fluid velocity.

Although this work introduces preliminary results, it successfully demonstrates the capability of the proposed numerical framework to capture the full dynamics of particle-fluid interactions in sediment transport. The model provides a powerful tool for studying particle-laden flows and offers a basis for developing constitutive laws that describe the rheological behavior of both the solid and fluid phases. While the Couette flow was used here for simplicity, future studies will consider Poiseuille flow to provide a more realistic representation of sediment transport in natural riverbeds and pipe flows.

It will be important to extend this work through a broader parametric study to gain deeper insights into bed load sediment transport. For instance, in a polydisperse granular bed, larger particles tend to migrate toward the bed surface, thereby shielding smaller particles from regions of higher flow velocity. This process leads to particle segregation in both bedload and creep regions. Investigating the segregation rates and contact orientation distribution of the force network represent an interesting direction for future research. Furthermore, the effect of particle shape and size on the fluid drag, lift forces, and the resulting bed load sediment flux remains an open and challenging question.

DECLARATION OF COMPETING INTEREST

The authors declare that there is no conflict of interest.

CREDIT AUTHOR STATEMENT

Duc Chung Vu: *Conceptualization, Methodology, Formal analysis, Validation, Investigation, Visualization, Writing-original draft, Writing-review & editing*. Thanh-Trung Vo: *Methodology, Investigation, Visualization, Writing-review & editing*.

FUNDING

This research received no specific grant from any funding agency in the public, commercial, or not-for-profit sectors.

REFERENCES

Amarsid, L., Delenne, J.-Y., Mutabaruka, P., Monerie, Y., Perales, F., & Radjai, F. (2017). Viscoinertial regime of immersed granular flows. *Physical Review E*, *96*(1), 012901. https://doi.org/10.1103/physreve.96.012901

Azéma, É., Radjaï, F., & Roux, J.-N. (2015). Internal friction and absence of dilatancy of packings of frictionless polygons. *Physical Review E*, *91*(1), 010202. https://doi.org/10.1103/physreve.91.010202

Azéma, É., Radjaï, F., & Roux, J.-N. (2018). Inertial shear flow of assemblies of frictionless polygons: Rheology and microstructure. *The European Physical Journal E*, *41*(1), 2. https://doi.org/10.1140/epje/i2018-11608-9

Bhatnagar, P. L., Gross, E. P., & Krook, M. (1954). A model for collision processes in gases. I. small amplitude processes in charged and neutral one-component systems. *Physical Review*, *94*(3), 511–525. https://doi.org/10.1103/physrev.94.511

Bigot, B., Bonometti, T., Lacaze, L., & Thual, O. (2014). A simple immersed-boundary method for solid–fluid interaction in constant- and stratified-density flows. *Computers & Fluids*, *97*, 126–142. https://doi.org/10.1016/j.compfluid.2014.03.030

Boton, M., Azéma, E., Estrada, N., Radjaï, F., & Lizcano, A. (2013). Quasistatic rheology and microstructural description of sheared granular materials composed of platy particles. *Physical Review E*, *87*(3), 032206. https://doi.org/10.1103/physreve.87.032206

Boutt, D. F., Cook, B. K., & Williams, J. R. (2011). A coupled fluid–solid model for problems in geomechanics: Application to sand production. *International Journal for Numerical and Analytical Methods in Geomechanics*, *35*(9), 997–1018. https://doi.org/10.1002/nag.938

Boutt, D. F., Cook, B. K., McPherson, B. J. O. L., & Williams, J. R. (2007). Direct simulation of fluid-solid mechanics in porous media using the discrete element and lattice-Boltzmann methods. *Journal of Geophysical Research: Solid Earth*, *112*(B10). https://doi.org/10.1029/2004jb003213

Bouzidi, M., Firdaouss, M., & Lallemand, P. (2001). Momentum transfer of a Boltzmann-lattice fluid with boundaries. *Physics of Fluids*, *13*(11), 3452–3459. https://doi.org/10.1063/1.1399290

Brilliantov, N. V., Spahn, F., Hertzsch, J.-M., & Pöschel, T. (1996). Model for collisions in granular gases. *Physical Review E*, *53*(5), 5382–5392. https://doi.org/10.1103/physreve.53.5382

Cantor, D., Azéma, E., & Preechawuttipong, I. (2020). Microstructural analysis of sheared polydisperse polyhedral grains. *Physical Review E*, *101*(6), 062901. https://doi.org/10.1103/physreve.101.062901

Charru, F., Mouilleron, H., & Eiff, O. (2004). Erosion and deposition of particles on a bed sheared by a viscous flow. *Journal of Fluid Mechanics*, *519*, 55–80. https://doi.org/10.1017/s0022112004001028

Cundall, P. A., & Strack, O. D. L. (1979). A discrete numerical model for granular assemblies. *Géotechnique*, *29*(1), 47–65. https://doi.org/10.1680/geot.1979.29.1.47

Deal, E., Venditti, J., Benavides, S., Bradley, R., Zhang, Q., Kamrin, K., & Perron, T. (2023). Grain shape effects in bed load sediment transport. *Nature*, *613*(7943), 298–302. https://doi.org/10.5194/egusphere-egu23-12076

Dedieu, B., Rousseau, H., Chauchat, J., & Frey, P. (2024). Exploring the size ratio impact on an intruder segregating in bedload transport. *Physical Review Fluids*, *9*(10), 104302. https://doi.org/10.1103/physrevfluids.9.104302

Derksen, J. J. (2011). Simulations of granular bed erosion due to laminar shear flow near the critical Shields number. *Physics of Fluids*, *23*(11), 113303. https://doi.org/10.1063/1.3660258

Di Renzo, A., & Di Maio, F. P. (2004). Comparison of contact-force models for the simulation of collisions in DEM-based granular flow codes. *Chemical Engineering Science*, *59*(3), 525–541. https://doi.org/10.1016/j.ces.2003.09.037

Elghannay, H. A., & Tafti, D. K. (2018). Sensitivity of numerical parameters on DEM predictions of sediment transport. *Particulate Science and Technology*, *36*, 438–446.

Feng, J., Hu, H. H., & Joseph, D. D. (1994). Direct simulation of initial value problems for the motion of solid bodies in a Newtonian fluid. Part 2. Couette and Poiseuille flows. *Journal of Fluid Mechanics*, *277*, 271–301. https://doi.org/10.1017/s0022112094002764

Feng, Y. T., Han, K., & Owen, D. R. J. (2007). Coupled lattice Boltzmann method and discrete element modelling of particle transport in turbulent fluid flows: Computational issues. *International Journal for Numerical Methods in Engineering*, *72*(9), 1111–1134. https://doi.org/10.1002/nme.2114

Feng, Z.-G., & Michaelides, E. E. (2004). The immersed boundary-lattice boltzmann method for solving fluid–particles interaction problems. *Journal of Computational Physics*, *195*(2), 602–628. https://doi.org/10.1016/j.jcp.2003.10.013

Frey, P., & Church, M. (2009). How river beds move. *Science*, *325*(5947), 1509–1510. https://doi.org/10.1126/science.1178516

Galindo-Torres, S. A. (2013). A coupled discrete element lattice Boltzmann method for the simulation of fluid–solid interaction with particles of general shapes. *Computer Methods in Applied Mechanics and Engineering*, *265*, 107–119. https://doi.org/10.1016/j.cma.2013.06.004

Gonzalez, J. O., Cúñez, F. D., & Franklin, E. M. (2023). Bidisperse beds sheared by viscous fluids: Grain segregation and bed hardening. *Physics of Fluids*, *35*(10), 103326. https://doi.org/10.1063/5.0168415

Gonzalez, J. O., & Franklin, E. M. (2024). Forces and grain–grain contacts in bidisperse beds sheared by viscous fluids. *Physics of Fluids*, *36*(11), 113342. https://doi.org/10.1063/5.0238582

Guazzelli, É., & Pouliquen, O. (2018). Rheology of dense granular suspensions. *Journal of Fluid Mechanics*, *852*, P1. https://doi.org/10.1017/jfm.2018.548

Han, K., Feng, Y. T., & Owen, D. R. J. (2007). Coupled lattice Boltzmann and discrete element modelling of fluid–particle interaction problems. *Computers & Structures*, *85*(11–14), 1080–1088. https://doi.org/10.1016/j.compstruc.2006.11.016

Han, Y., & Cundall, P. A. (2013). LBM–DEM modeling of fluid-solid interaction in porous media. *International Journal for Numerical and Analytical Methods in Geomechanics*, *37*, 1391–1407.

Harshani, H. M. D., Galindo-Torres, S. A., Scheuermann, A., & Muhlhaus, H. B. (2015). Micro-mechanical analysis on the onset of erosion in granular materials. *Philosophical Magazine*, *95*(28–30), 3146–3166. https://doi.org/10.1080/14786435.2015.1049237

He, X., & Luo, L.-S. (1997a). A priori derivation of the lattice Boltzmann equation. *Physical Review E*, *55*(6), R6333–R6336. https://doi.org/10.1103/physreve.55.r6333

He, X., & Luo, L.-S. (1997b). Theory of the lattice Boltzmann method: From the Boltzmann equation to the lattice Boltzmann equation. *Physical Review E*, *56*(6), 6811–6817. https://doi.org/10.1103/physreve.56.6811

Ismail, K. A., & Stronge, W. J. (2008). Impact of viscoplastic bodies: Dissipation and restitution. *Journal of Applied Mechanics*, *75*(6). https://doi.org/10.1115/1.2965371

Ji, C., Munjiza, A., Avital, E., Ma, J., & Williams, J. J. R. (2013). Direct numerical simulation of sediment entrainment in turbulent channel flow. *Physics of Fluids*, *25*(5), 056601. https://doi.org/10.1063/1.4807075

Ji, C., Munjiza, A., Avital, E., Xu, D., & Williams, J. (2014). Saltation of particles in turbulent channel flow. *Physical Review E*, *89*(5), 052202. https://doi.org/10.1103/physreve.89.052202

Krüger, T., Kusumaatmaja, H., Kuzmin, A., Shardt, O., Silva, G., & Viggen, E. M. (2017). *The lattice boltzmann method: Principles and practice* (Vol. 10). Springer International Publishing. https://doi.org/10.1007/978-3-319-44649-3

Ladd, A. J. C., & Verberg, R. (2001). Lattice-Boltzmann simulations of particle-fluid suspensions. *Journal of Statistical Physics*, *104*(5), 1191–1251. https://doi.org/10.1023/a:1010414013942

Ladd, A. J. C. (1994). Numerical simulations of particulate suspensions via a discretized Boltzmann equation. Part 1. theoretical foundation. *Journal of Fluid Mechanics*, *271*, 285–309. https://doi.org/10.1017/s0022112094001771

Lallemand, P., & Luo, L.-S. (2000). Theory of the lattice Boltzmann method: Dispersion, dissipation, isotropy, Galilean invariance, and stability. *Physical Review E*, *61*(6), 6546–6562. https://doi.org/10.1103/physreve.61.6546

Lallemand, P., & Luo, L.-S. (2003). Lattice Boltzmann method for moving boundaries. *Journal of Computational Physics*, *184*(2), 406–421. https://doi.org/10.1016/s0021-9991(02)00022-0

Li, J., Yu, A., Bridgwater, J., & Rough, S. (2010). Spontaneous inter-particle percolation: A kinematic simulation study. *Powder Technology*, *203*(2), 397–403. https://doi.org/10.1016/j.powtec.2010.05.037

Lominé, F., Scholtès, L., Sibille, L., & Poullain, P. (2013). Modeling of fluid–solid interaction in granular media with coupled lattice Boltzmann/discrete element methods: Application to piping erosion. *International Journal for Numerical and Analytical Methods in Geomechanics*, *37*, 577–596.

Louge, M. Y. (1994). Computer simulations of rapid granular flows of spheres interacting with a flat, frictional boundary. *Physics of Fluids*, *6*(7), 2253–2269. https://doi.org/10.1063/1.868178

Mansouri, M., Delenne, J.-Y., Seridi, A., & El Youssoufi, M. S. (2011). Numerical model for the computation of permeability of a cemented granular material. *Powder Technology*, *208*(2), 532–536. https://doi.org/10.1016/j.powtec.2010.08.055

Masteller, C. C., & Finnegan, N. J. (2017). Interplay between grain protrusion and sediment entrainment in an experimental flume. *Journal of Geophysical Research: Earth Surface*, *122*(1), 274–289. https://doi.org/10.1002/2016jf003943

Masteller, C. C., Finnegan, N. J., Turowski, J. M., Yager, E. M., & Rickenmann, D. (2019). History-dependent threshold for motion revealed by continuous bedload transport measurements in a steep mountain stream. *Geophysical Research Letters*, *46*(5), 2583–2591. https://doi.org/10.1029/2018gl081325

Müller, P., Krengel, D., & Pöschel, T. (2012). Negative coefficient of normal restitution. *Physical Review E*, *85*(4), 041306. https://doi.org/10.1103/physreve.85.041306

Mussa, A., Asinari, P., & Luo, L.-S. (2009). Lattice Boltzmann simulations of 2D laminar flows past two tandem cylinders. *Journal of Computational Physics*, *228*(4), 983–999. https://doi.org/10.1016/j.jcp.2008.10.010

Mutabaruka, P., Delenne, J.-Y., Soga, K., & Radjai, F. (2014). Initiation of immersed granular avalanches. *Physical Review E*, *89*(5), 052203. https://doi.org/10.1103/physreve.89.052203

Ngoma, J., Philippe, P., Bonelli, S., Radjaï, F., & Delenne, J.-Y. (2018). Two-dimensional numerical simulation of chimney fluidization in a granular medium using a combination of discrete element and lattice Boltzmann methods. *Physical Review E*, *97*(5), 052902. https://doi.org/10.1103/physreve.97.052902

Nguyen, T.-K., Nguyen, N. H. T., Vo, T.-T., & Chen, L. (2025). Dissipative effects of baffles on the dynamics of debris flow and its impact on downstream structure. *Computers and Geotechnics*, *184*, 107246. https://doi.org/10.1016/j.compgeo.2025.107246

Niu, X. D., Shu, C., Chew, Y. T., & Peng, Y. (2006). A momentum exchange-based immersed boundary-lattice Boltzmann method for simulating incompressible viscous flows. *Physics Letters A*, *354*(3), 173–182. https://doi.org/10.1016/j.physleta.2006.01.060

Owen, D. R. J., Leonardi, C. R., & Feng, Y. T. (2011). An efficient framework for fluid-structure interaction using the lattice Boltzmann method and immersed moving boundaries. *International Journal for Numerical Methods in Engineering*, *87*, 66–95.

Pähtz, T., Clark, A. H., Valyrakis, M., & Durán, O. (2020). The physics of sediment transport initiation, cessation, and entrainment across aeolian and fluvial environments. *Reviews of Geophysics*, *58*(1), e2019RG000679. https://doi.org/10.1029/2019rg000679

Peng, C., Teng, Y., Hwang, B., Guo, Z., & Wang, L.-P. (2016). Implementation issues and benchmarking of lattice Boltzmann method for moving rigid particle simulations in a viscous flow. *Computers & Mathematics with Applications*, *72*(2), 349–374. https://doi.org/10.1016/j.camwa.2015.08.027

Radjai, F., & Dubois, F. (2011). *Discrete-element modeling of granular materials*. Wiley-Iste.

Raymond Pralong, M., Turowski, J. M., Rickenmann, D., & Zappa, M. (2015). Climate change impacts on bedload transport in alpine drainage basins with hydropower exploitation. *Earth Surface Processes and Landforms*, *40*(12), 1587–1599. https://doi.org/10.1002/esp.3737

Schmeeckle, M. W. (2014). Numerical simulation of turbulence and sediment transport of medium sand. *Journal of Geophysical Research: Earth Surface*, *119*(6), 1240–1262. https://doi.org/10.1002/2013jf002911

Succi, S. (2018, April). *The lattice Boltzmann equation: For complex states of flowing matter*. Oxford University Press. https://doi.org/10.1093/oso/9780199592357.001.0001

Tang, H., Song, R., Dong, Y., & Song, X. (2019). Measurement of restitution and friction coefficients for granular particles and discrete element simulation for the tests of glass beads. *Materials*, *12*(19), 3170. https://doi.org/10.3390/ma12193170

van der Hoef, M. A., van Sint Annaland, M., Deen, N. G., & Kuipers, J. A. M. (2008). Numerical simulation of dense gas-solid fluidized beds: A multiscale modeling strategy. *Annual Review of Fluid Mechanics*, *40*(1), 47–70. https://doi.org/10.1146/annurev.fluid.40.111406.102130

Vo, T. T., Nezamabadi, S., Mutabaruka, P., Delenne, J.-Y., & Radjai, F. (2020). Additive rheology of complex granular flows. *Nature Communications*, *11*(1), 1476. https://doi.org/10.1038/s41467-020-15263-3

Vo, T.-T., Tran, D. M., Nguyen, C. T., & Nguyen, T.-K. (2023). Discrete element investigation of the mobility of granular mass flows. *Solid State Communications*, *369*, 115190. https://doi.org/10.1016/j.ssc.2023.115190

Vu, D. C., Amarsid, L., Delenne, J.-Y., Richefeu, V., & Radjai, F. (2023). Macro-elasticity of granular materials composed of polyhedral particles. *Granular Matter*, *26*(1), 6. https://doi.org/10.1007/s10035-023-01382-3

Vu, D. C., Amarsid, L., Delenne, J.-Y., Richefeu, V., & Radjai, F. (2024a). Rheology and scaling behavior of polyhedral particle flows in rotating drums. *Powder Technology*, *434*, 119338. https://doi.org/10.1016/j.powtec.2023.119338

Vu, D. C., Amarsid, L., Delenne, J.-Y., Richefeu, V., & Radjai, F. (2024b). Particle fracture regimes from impact simulations. *Physical Review E*, *109*(4), 044907. https://doi.org/10.1103/physreve.109.044907

Vu, D. C., Amarsid, L., Richefeu, V., Delenne, J.-Y., & Radjai, F. (2025). Quasistatic rheology of granular materials composed of dodecahedra. *The European Physical Journal Special Topics*. https://doi.org/10.1140/epjs/s11734-025-01907-2

Wen, B., Zhang, C., Tu, Y., Wang, C., & Fang, H. (2014). Galilean invariant fluid–solid interfacial dynamics in lattice boltzmann simulations. *Journal of Computational Physics*, *266*, 161–170. https://doi.org/10.1016/j.jcp.2014.02.018

Zhang, B., Xu, D., Zhang, B., Ji, C., Munjiza, A., & Williams, J. (2020). Numerical investigation on the incipient motion of non-spherical sediment particles in bedload regime of open channel flows. *Computational Particle Mechanics*, *7*(5), 987–1003. https://doi.org/10.1007/s40571-020-00323-8

Zou, Q., & He, X. (1997). On pressure and velocity boundary conditions for the lattice Boltzmann BGK model. *Physics of Fluids*, *9*(6), 1591–1598. https://doi.org/10.1063/1.869307